metals

MDPI

Article

High-Temperature Mechanical Behavior of Cobalt-Free FeMnCrNi(Al) High-Entropy Alloys

Dan Liu [1,2], Xi Jin [1], Huijun Yang [1], Junwei Qiao [1,2,*] and Yong Zhang [3,*]

[1] Laboratory of High-Entropy Alloys, College of Materials Science and Engineering, Taiyuan University of Technology, Taiyuan 030024, China; liudan217@hotmail.com (D.L.)
[2] Key Laboratory of Interface Science and Engineering in Advanced Materials, Ministry of Education, Taiyuan University of Technology, Taiyuan 030024, China
[3] Beijing Advanced Innovation Center of Materials Genome Engineering, State Key Laboratory for Advanced Metals and Materials, University of Science and Technology Beijing, Beijing 100083, China
* Correspondence: qiaojunwei@gmail.com (J.Q.); drzhangy@ustb.edu.cn (Y.Z.)

Abstract: The high-temperature properties of new alloys need to be investigated to guide the hot working process. The temperature sensitivity of various microstructures of $Fe_{45}Mn_{15}Cr_{15}Ni_{25}$ and $Fe_{35}Mn_{15}Cr_{15}Ni_{25}Al_{10}$ cobalt-free high-entropy alloys was investigated using high-temperature tensile tests. For recrystallized alloys, the increase in aluminum (Al) atoms exacerbates the emergence of serration behavior, prolongs the strain hardening capacity, and delays the decrease in plasticity. The $Fe_{35}Mn_{15}Cr_{15}Ni_{25}Al_{10}$ alloy, with a high-density precipitated phase, exhibits excellent mechanical properties at 673 K. It has a yield strength of 735 MPa, an ultimate tensile strength of 1030 MPa, and an elongation of 11%. Ultimately, it has been found that the addition of the element Al improves the strength, oxidation resistance, and thermal stability of the alloy. According to the solid solution strengthening model fitting and nanoindentation results, the temperature sensitivity of the yield strength of the alloy is primarily attributed to the solid solution strengthening and phase interface forces. There is relatively less variation in grain boundary strengthening and precipitation strengthening. The relationship between the mechanical properties and temperature of the alloy can be predicted to guide the machining process of the alloy.

Keywords: high-entropy alloys; high temperature; tensile properties; serration behavior; temperature sensitivity

Citation: Liu, D.; Jin, X.; Yang, H.; Qiao, J.; Zhang, Y. High-Temperature Mechanical Behavior of Cobalt-Free FeMnCrNi(Al) High-Entropy Alloys. *Metals* **2023**, *13*, 1885. https://doi.org/10.3390/met13111885

Academic Editor: Martin Heilmaier

Received: 22 September 2023
Revised: 20 October 2023
Accepted: 8 November 2023
Published: 13 November 2023

1. Introduction

The discovery of high-entropy alloys (HEAs) was a breakthrough in the field of materials and provided us with a wide range of options to expand our choices for achieving desired alloy compositions [1–4]. Many HEAs with excellent properties have been developed. As an example, the face-centered cubic (FCC) CoCrFeMnNi HEA has been widely studied due to its superior ductility and damage tolerance at both room temperature and low temperatures [5,6]. Moreover, the mechanical behavior at high temperatures was also investigated to determine the effect of the thermal processing temperature [7,8]. In a comprehensive study, the quantitative relationship between milling temperature and milling speed in $CoCrFeNiAl_X$ high-entropy alloys was established [9]. The high-entropy effect was found to achieve excellent oxygen barrier performance in other studies [10]. The establishment of the processing–microstructure–properties relationship is necessary for material development.

Currently, extensive research is being conducted on low-cost cobalt-free high-entropy alloys. In the development of cobalt-free HEAs, numerous special structures and compositions with excellent comprehensive mechanical properties have been reported [11–13]. However, little attention has been given to the thermal deformation of these HEAs. The mechanical behavior and thermal stability of HEAs at high temperatures are still unclear.

These must be taken into account during the manufacturing process. This type of low-cost alloy requires more fundamental data to develop new alloys with even better properties.

Additionally, the precipitated phase and aluminum elements have an important impact on the high-temperature properties of the alloys [14,15]. The addition of aluminum (Al) elements could promote dislocation nucleation and improve the strength and plasticity of the alloy [16,17]. Furthermore, the presence of the element Al increases the oxidation resistance of the alloys [18]. The $AlCoCrFeNi_{2.1}$ eutectic high-entropy alloy, composed of the ordered FCC phase ($L1_2$) and the ordered body-centered cubic phase (B2), exhibits exceptional mechanical properties at temperatures below 973 K [19]. However, the temperature sensitivity of semi-coherent body-centered cubic (BCC) or B2 precipitates remains uncertain.

Therefore, it is of great interest to investigate the high-temperature mechanical behavior of cobalt-free FeMnCrNi(Al) HEAs. The $Fe_{45}Mn_{15}Cr_{15}Ni_{25}$ and $Fe_{35}Mn_{15}Cr_{15}Ni_{25}Al_{10}$ (in at.%) HEAs developed in the early stage of research were selected for the current research [11]. The control groups for the element Al and precipitated phase were set separately. This study will investigate the relationship between mechanical behavior and microstructural evolution during hot tensile tests, focusing on the influence of deformation temperatures. At the same time, constitutive equations for yield strength were also developed to predict the trend of alloy properties.

2. Materials and Methods

Alloy ingots with nominal compositions of $Fe_{45}Mn_{15}Cr_{15}Ni_{25}$ (Al0) and $Fe_{35}Mn_{15}Cr_{15}Ni_{25}Al_{10}$ (Al10) (in at.%) were prepared through arc melting a mixture of metallic elements in a high-purity argon atmosphere. The purity of each raw material was at least 99.9 wt.%. The as-cast ingots were subjected to homogenization, cold rolling (CR), and then recrystallization annealing at 1273 K for 1 h and 1473 K for 10 min, respectively. The specimens are referred to as R1273 and R1473, respectively. The third alloy containing high-density precipitates was obtained by aging after R1473 at 973 K for 10 h, named A973. The cooling method used in the final heat treatment mentioned above was air cooling. The pretreatment processes in this study were all used due to the previous research results.

Tensile tests were performed using an Instron 5969 (Instron, a Division of Illinois ToolWorks Inc. ITW, Norwood, MA, USA) machine at a constant strain rate of 1×10^{-3} s^{-1} at room temperature (293 K) and other temperatures. Dog-bone-shaped specimens with gauge dimensions of 13 mm (length) × 3 mm (width) × 0.7 mm (thickness) were prepared. The samples were rapidly heated to a specific temperature (473, 673, 873, and 1073 K) ±10 K using a Thermo Riko (Tokyo, Japan)/GA298 infrared lamp heating device, held for 5 min, and then stretched. All tensile tests were repeated at least three times to ensure the reliability and reproducibility of the results. The microstructure, fracture morphologies, and elemental analysis were investigated using a Phenom XL (Phenom-World BV, Eindhoven, The Netherlands) scanning electron microscope (SEM) equipped with an energy dispersive spectrometer (EDS). Nanoindentation (Bruker, Minneapolis, MN, USA) experiments were performed for H1473 samples at room temperature using a Berkovich diamond indenter. The nanohardness tests were conducted at a constant loading rate of 1.6 mN/s with a peak load of 8 mN.

3. Results

3.1. Initial Microstructures

Figure 1a–c show the SEM morphologies of R1273, R1473, and A973, respectively. The $Fe_{45}Mn_{15}Cr_{15}Ni_{25}$ (Al0) alloy is a single-phase recrystallized microstructure with an average grain size of approximately 30 μm. The recrystallized matrix of the $Fe_{35}Mn_{15}Cr_{15}Ni_{25}Al_{10}$ (Al10) alloy contains a small amount of secondary precipitated phase, and its grain size is about 39 μm. The second-phase particles are a bulk NiAl-B2 phase with a size of 4 μm, accounting for 3.7%. In contrast, the A973 sample contains 24.4% of precipitated phases such as NiAl-B2 and Cr-rich phases, ranging in size from 20 nm to 4 μm. Secondary

precipitated phases exist both at grain boundaries and within the grains. The size of the precipitated phase on the grain boundary is approximately 400 nm, while the size of the precipitated phase within the grain is around 130 nm. This portion of the precipitated phase accounts for 16.7%. The results of the statistics were derived from previous studies [11]. The main difference between R1273 and R1473 lies in the Al content, while A973 and R1473 are distinguished by the content of the precipitated phase. Table 1 presents the atomic percentage chemical composition of the FCC matrix in the studied alloys. The composition of the alloy is in the final state.

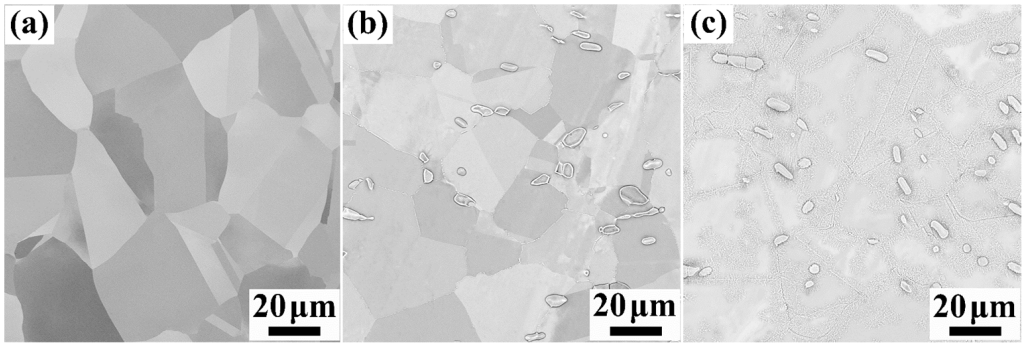

Figure 1. SEM morphologies of R1273, R1473, and A973 samples at (**a**) Al0 1273 K 1 h, (**b**) Al10 1473 K 10 min, and (**c**) Al10 1473 K 10 min + 973 K 10 h, respectively.

Table 1. The chemical composition of the studied alloys in atomic percent (at.%).

Alloy	Fe	Ni	Cr	Mn	Al
$Fe_{45}Mn_{15}Cr_{15}Ni_{25}$ (R1273)	$45.26^{+0.05}_{-0.13}$	$25.06^{+0.09}_{-0.06}$	$14.86^{+0.04}_{-0.05}$	$14.89^{+0.09}_{-0.07}$	-
$Fe_{35}Mn_{15}Cr_{15}Ni_{25}Al_{10}$ (R1473)	$37.03^{+0.15}_{-0.11}$	$24.74^{+0.13}_{-0.08}$	$14.83^{+0.09}_{-0.03}$	$14.63^{+0.14}_{-0.08}$	$8.77^{+0.07}_{-0.04}$
$Fe_{35}Mn_{15}Cr_{15}Ni_{25}Al_{10}$ (A973)	$37.29^{+0.13}_{-0.11}$	$24.76^{+0.03}_{-0.09}$	$14.71^{+0.05}_{-0.09}$	$15.04^{+0.08}_{-0.05}$	$8.2^{+0.03}_{-0.07}$

3.2. Tensile Properties

Figure 2 illustrates the engineering stress–strain curves of the R1273, R1473, and A973 alloys at different temperatures, and the changes in yield strength ($\sigma_{0.2}$), ultimate strength (σ_u), and total elongation (ε_u) are summarized. The specific values of Figure 2(a_1–c_1) are listed in Table 2. Table 2 presents the tensile properties of the studied alloys at both room temperature and elevated temperatures. The decreasing trend of the yield strength in the R1273 and R1473 alloys was similar as the temperature increased. The yield strength of the R1273 alloy decreased from 190 MPa to 85 MPa, while the yield strength of the R1473 alloy decreased from 255 MPa to 140 MPa. However, the elongation of the R1473 alloy decreased at a slower rate compared to the R1273 alloy. The plasticity of the R1473 alloy at 473 K and 673 K was even higher than at room temperature. This indicates that the addition of aluminum (Al) not only enhances the oxidation resistance of the alloy but also improves its thermal stability. The yield strength and ultimate tensile strength of the alloys in Figure 2(a_1,b_1) almost coincided at 1073 K, indicating that thermal softening occurs at high temperatures. The onset temperature of thermal softening for the R1273 and R1473 alloys was around 1073 K.

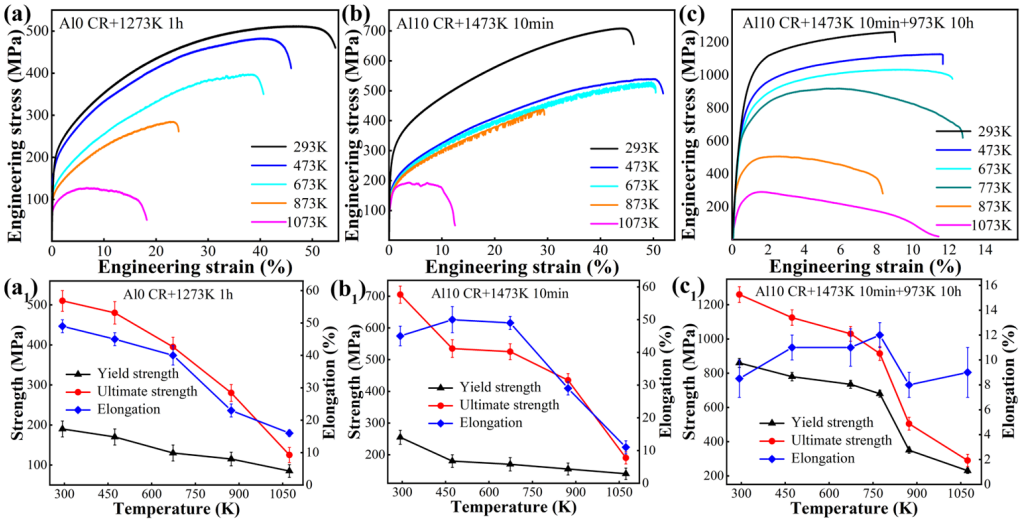

Figure 2. The engineering stress–strain curves of Al0 and Al10 alloys at different temperatures, as well as the changes in yield strength, ultimate strength, and total elongation, are summarized: (**a**,**a**$_1$) Al0 CR + 1273 K 1 h, (**b**,**b**$_1$) Al10 CR + 1473 K 10 min, and (**c**,**c**$_1$) Al10 CR + 1473 K 10 min + 973 K 10 h.

Table 2. Tensile properties of the investigated alloys at both ambient and elevated temperatures.

Composition	Temperatures (K)	$\sigma_{0.2}$ (MPa)	σ_{UTS} (MPa)	ε_u (%)
$Fe_{45}Mn_{15}Cr_{15}Ni_{25}$ (R1273)	293	190 ± 20	510 ± 26	49 ± 2
	473	170 ± 20	480 ± 28	45 ± 2
	673	130 ± 20	395 ± 24	40 ± 3
	873	115 ± 17	280 ± 21	23 ± 2
	1073	85 ± 16	125 ± 19	16 ± 1
$Fe_{35}Mn_{15}Cr_{15}Ni_{25}Al_{10}$ (R1473)	293	255 ± 22	705 ± 17	45 ± 3
	473	180 ± 20	535 ± 28	50 ± 4
	673	170 ± 21	525 ± 25	49 ± 2
	873	155 ± 19	435 ± 21	29 ± 2
	1073	140 ± 18	190 ± 19	11 ± 2
$Fe_{35}Mn_{15}Cr_{15}Ni_{25}Al_{10}$ (A973)	293	860 ± 26	1260 ± 46	9 ± 1
	473	780 ± 25	1125 ± 45	11 ± 1
	673	735 ± 23	1030 ± 43	11 ± 2
	773	680 ± 20	915 ± 40	12 ± 1
	873	350 ± 18	505 ± 38	8 ± 1
	1073	230 ± 16	290 ± 36	9 ± 2

In contrast, the A973 alloy, which contained high-density precipitated phases, began to significantly soften at 773 K, and then the strength of the alloy decreased remarkably at 873 K. Excellent comprehensive mechanical properties were obtained at 673 K, with a yield strength of 735 MPa, an ultimate tensile strength of 1030 MPa, and an elongation of 11%.

The early softening temperature of the A973 sample should be related to the precipitation of the secondary phase. The increase in the temperature leads to a decrease in the interaction force between the two phases, a significant weakening of the back-stress hardening, and subsequently a decrease in the strength and strain hardening capability of the alloy [20]. The relationship between elongation and temperature of the A973 alloy is nonlinear, which distinguishes it from the recrystallization alloy mentioned above. At 1073 K, the work-hardening ability of the A973 alloy almost completely disappeared, and the total elongation increased. The softening of the alloy at this point was entirely dominant.

In addition, Figure 3 shows the serrated flow behaviors, and the stress fluctuation phenomenon during the plastic deformation was observed on the high-temperature tensile curves of the R1273 and R147 alloys. For the R1273 alloy, serrations only appeared at 673 K,

whereas for the R1473 alloy, serrations occurred between 473 K and 873 K. The R1273 HEA only exhibited type-A serrations with a gradually increasing amplitude, as shown in Figure 3a–c. The type-A serrations had upward spikes above the average flow stress [21]. The R1473 HEA began to show type-A serrations at the later stage of deformation at 473 K. Figure 3e–h exhibit the serrated type of R1473 alloy at 673 K ranges from A to A + B, B, and until fracture. The frequency of the serrations always increased. Type-B serration had a uniform frequency and amplitude, which may be favorable for alloy plasticity [22,23]. The plasticity of the R1473 alloy slowly decreased. Figure 3i indicates that the R1473 alloy exhibited type-C serrations at 873 K. These type-C serrations featured stress drops below the average flow stress level, which typically occur at elevated temperatures [22]. It has been suggested that the occurrence of serrated plastic deformation is likely related to the propensity for cross-slip [24]. The types of serrations are usually related to the deformation mechanism and solute drag effect [24,25]. Therefore, the A973 sample did not show serrations during high-temperature deformation, probably due to the presence of the secondary phase weakening the solute drag effect. The interaction between the precipitated phases and dislocations was more apparent.

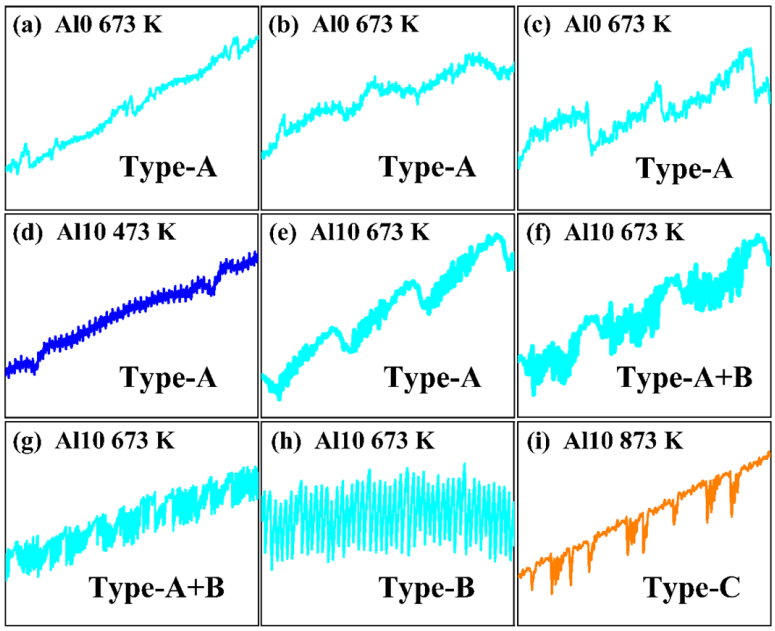

Figure 3. Enlarged segments of stress–strain curves are shown in Figure 2a,b; (**a**–**c**) the flow behavior at 673 K only features type-A serrations in R1273 HEA; and (**d**–**i**) the flow behavior features type-A, type-B, and type-C serrations in R1473 HEA.

Furthermore, the comparison of the yield strength, ultimate tensile strength, and elongation at various temperatures in the present study and other alloys is presented in Figure 4 [19,25–31]. The reference values are shown in Supplementary Table S1. For the single-phase alloys investigated in this study, the mechanical properties and temperature sensitivity are comparable to those of FCC alloys, such as CoCrFeMnNi HEAs and 316SS stainless steels. Judging from the strength reduction factors ($k_{0.2} = \sigma_{0.2,\,T}/\sigma_{0.2}$ and $k_u = \sigma_{u,\,T}/\sigma_u$), these can be comparable to certain duplex stainless steels and superior to some austenitic stainless steels [32]. This also indicates that the addition of the element Al enhances the thermal stability of the alloy. The A973 alloy has high strengths below 673 K, approaching that of the coherent nanoprecipitation-strengthened superalloys and several eutectic alloys [19,26,28]. However, the thermal stability of the alloy is poor, and the properties of the alloy considerably decrease after 673 K. The thermal stability of the semi-coherent interface is much worse than that of the coherent interface. Therefore, the alloys studied here are only suitable for medium and low-temperature environments.

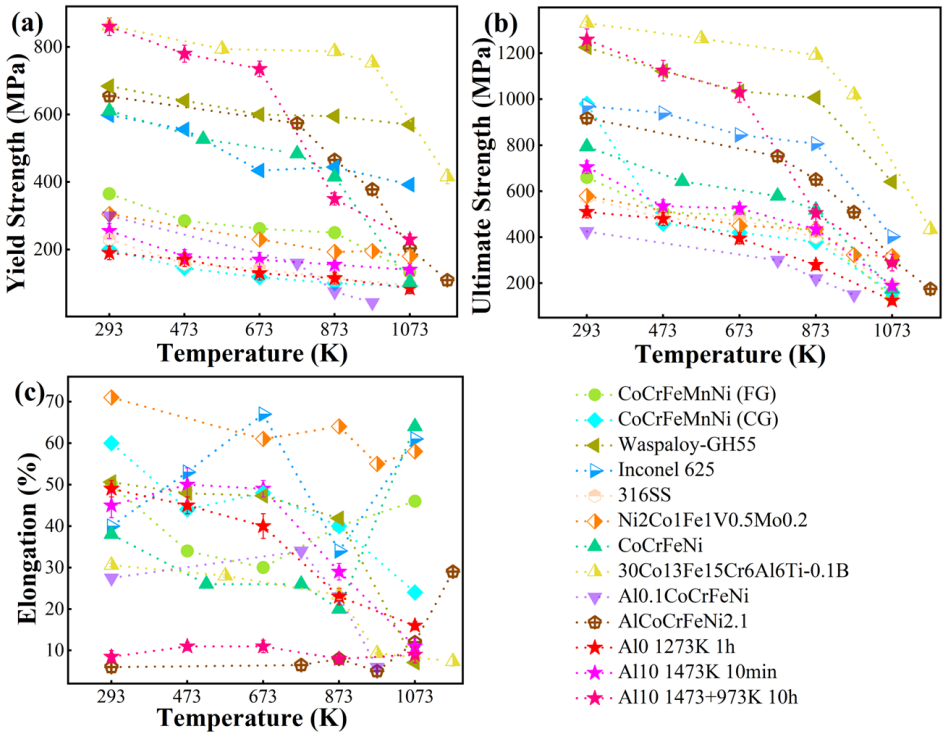

Figure 4. Comparison of this work with other alloys in terms of yield strength, ultimate tensile strength, and elongation at various temperatures [19,25–31]. (**a**) yield strength vs. temperatures; (**b**) ultimate strength vs. temperatures; (**c**) elongation vs. temperatures.

3.3. Fracture Characteristics

Figure 5 presents the fracture morphologies of the tensile specimen at different temperatures. With the increase in the temperatures, the fracture mode changes from ductile fracture to intergranular fracture. The fracture features of the alloy are dimples from room temperature to 873 K. The fracture mode of the R1273 and R1473 alloys changed at 873 K, exhibiting fewer dimples, intergranular fracture, and the presence of some fine particles.

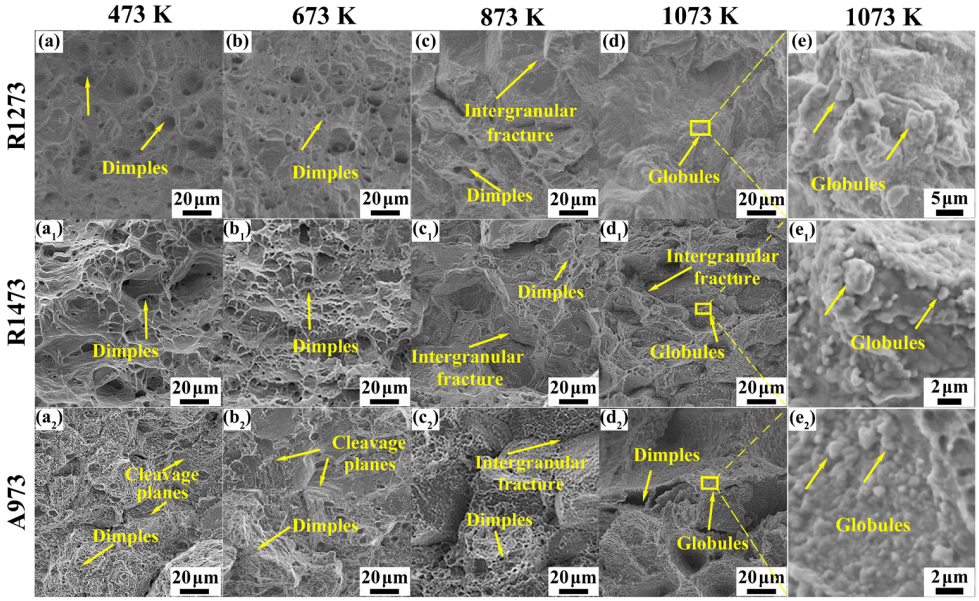

Figure 5. SEM images of the fracture morphologies of R1273, R1473, and A973 tensile samples at (**a**–**a$_2$**) 473 K, (**b**–**b$_2$**) 673 K, (**c**–**c$_2$**) 873 K, and (**d**–**d$_2$**) 1073 K, respectively; (**e**–**e$_2$**) show partially enlarged graphs of (**d**–**d$_2$**), respectively.

The intergranular fracture is related to the embrittlement of the alloy at medium temperatures [31]. More globules were formed at 1073 K, which may be due to dynamic recrystallization occurring at the crack tip [25]. Figure 5(e–e_2) show partially enlarged graphs of Figure 5(d–d_2), respectively. It shows the globules more clearly. The partial melting phenomenon of the R1273 alloy is more severe than that of the R1473 alloy. The A973 alloy has always exhibited a mixed fracture mode characterized by cleavage planes and dimples. Intergranular fracture occurs at 873 K, while globules form at 1073 K. At 1073 K, it undergoes a complete transformation into a ductile fracture, and the dimples become noticeably larger. This is consistent with the softening in mechanical properties observed at 1073 K. In other words, the impact of temperature on fracture characteristics is highly pronounced.

Additionally, the oxidation of the alloy was found on the fracture surface. Figure 6 illustrates the presence of oxides and newly generated NiAl precipitates at the fracture site of the tensile specimens of the R1473 alloy at 1073 K. The oxide is only present on the fracture surface. Moreover, it was observed that the alloy began to oxidize at 873 K, resulting in a blackened fracture surface. Oxide particles also contribute to embrittlement at medium temperatures. On the other hand, the plasticity of the R1473 alloy decreases less than that of the R1273 alloy, indicating that the presence of the element Al affects the oxidation resistance. At the same temperature, the oxidation degree of the R1473 alloy is lower than that of the R1273 alloy. Correspondence with Figure 5(e–e_2) reveals that the coarse globules consist mostly of oxides, whereas the smaller particles are precipitated phases. Combined with the results of tensile testing, the formation of fine precipitates during the tensile process enhances the occurrence of serrations. It improves the work-hardening capacity of Al-added alloys and has little effect on their plasticity. The high-temperature mechanical properties of the A973 alloy also show that the high-density precipitates do not aggravate the occurrence of stress concentration at high temperatures. In conclusion, the addition of the element Al enhances the oxidation resistance of the alloy and slows down the degradation of its mechanical properties.

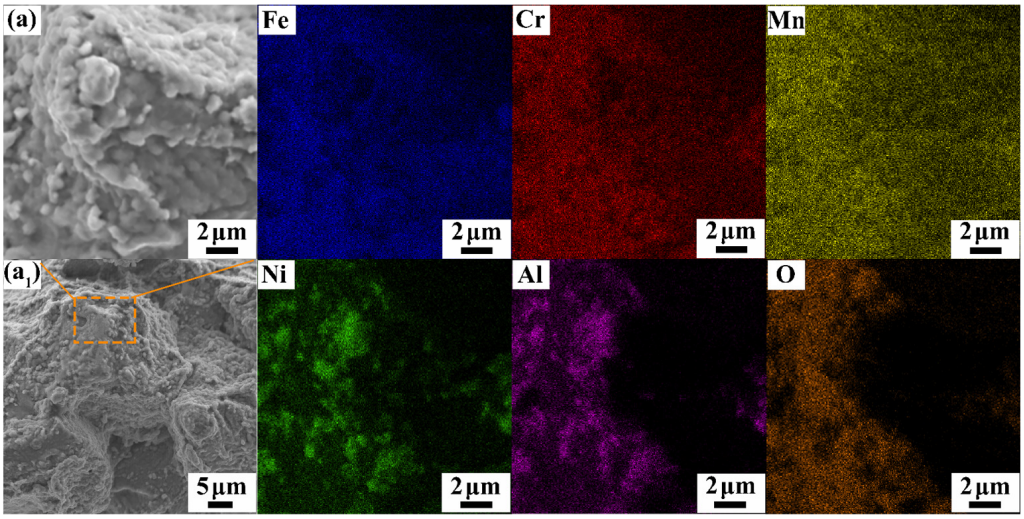

Figure 6. The SEM images and EDS mappings of the fracture tips of the R1473 post-tensile specimen at 1073 K; (**a**$_1$) shows a partially enlarged graph of (**a**).

Figure 7 presents the post-fracture cross-sectional morphologies of the three samples at 1073 K. The R1273 alloy displayed a clear dynamic recrystallization phenomenon, as seen in Figure 7a. The recrystallized grain size was about 3.6 μm. However, there were only a large number of crossed slip bands in the R1473 alloy, and no dynamic recrystallization was found. Cross networks are the core of dynamic recrystallization [33,34]. In fact, the recrystallization temperature of the $Fe_{45}Mn_{15}Cr_{15}Ni_{25}$ alloy was much lower than that of the $Fe_{35}Mn_{15}Cr_{15}Ni_{25}Al_{10}$ alloy in previous studies. The morphology of the A973

alloy is dominated by grain elongation, with a small amount of slip bands, indicating the presence of grain growth. These characteristics correspond to the mechanical properties. The mechanical characteristics of the $Fe_{35}Mn_{15}Cr_{15}Ni_{25}Al_{10}$ alloy are significantly different from those of single-phase alloys because of the presence of high-density semi-coherent precipitates. In addition, black microcracks appeared on the fracture surface. The majority of them were distributed on the grain boundaries, which was consistent with the intergranular fracture characteristics at high temperatures. The stress concentration at high temperatures is more inclined to occur at the grain boundaries. The effect of dislocations on the phase interface is weakened at high temperatures.

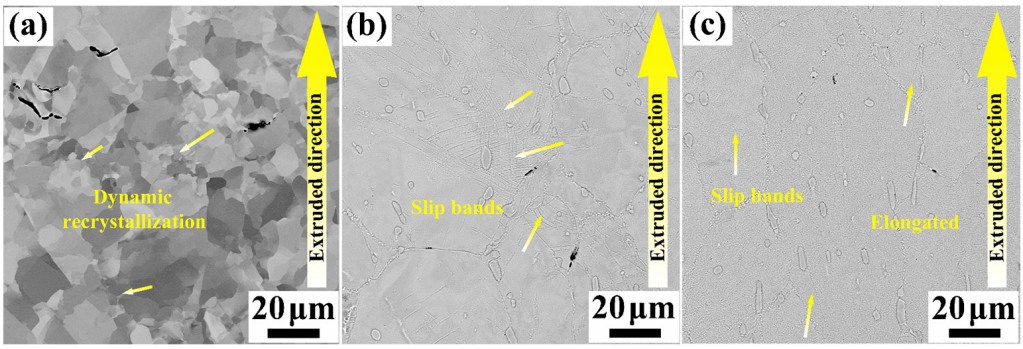

Figure 7. The post-fracture cross-sectional morphologies of the three samples were observed at 1073 K: (**a**) Al0 1273 K 1 h, (**b**) Al10 1473 K 10 min, and (**c**) Al10 1473 K 10 min + 973 K 10 h. The arrow indicates the extruded direction.

4. Discussion

The temperature sensitivity of the yield strength varies among the three alloys. To better highlight the temperature dependencies of the yield strength, the experimental data were fitted using the solid solution strengthening model proposed by Varvenne et al. The temperature-dependent flow stress ($\sigma_y(T, \dot{\varepsilon})$) is given by [35,36] the following:

$$\sigma_y(T, \dot{\varepsilon}) = M \cdot \tau_{y0} \left[1 - \left(\frac{kT}{\Delta E_b} \ln \frac{\dot{\varepsilon}_0}{\dot{\varepsilon}} \right)^{\frac{2}{3}} \right] \quad (1)$$

Here, M = 3.06 (FCC); T and $\dot{\varepsilon} = 10^{-3}$ s^{-1} are the temperature and strain rate of the test, respectively; τ_{y0} is the shear stress at 0 K; $\dot{\varepsilon}_0$ is a reference strain rate with a value of 10^4 s^{-1}; k = 1.3806 × 10^{-23} J/K which is the Boltzmann constant; and ΔE_b is the energy barrier of thermal activation. τ_{y0} and ΔE_b can be, respectively, written as follows [35,37]:

$$\tau_{y0} = 0.051 \alpha^{-\frac{1}{3}} \mu \left(\frac{1+\nu}{1-\nu} \right)^{\frac{4}{3}} f_1(w_c) \left[\frac{\sum_n c_n \left(\Delta \overline{V}_n^2 + \sigma_{\Delta V_n}^2 \right)}{b^6} \right]^{\frac{2}{3}} \quad (2)$$

$$\Delta E_b = 0.274 \alpha^{\frac{1}{3}} \mu b^3 \left(\frac{1+\nu}{1-\nu} \right)^{\frac{2}{3}} f_2(w_c) \left[\frac{\sum_n c_n \left(\Delta \overline{V}_n^2 + \sigma_{\Delta V_n}^2 \right)}{b^6} \right]^{\frac{1}{3}} \quad (3)$$

where α = 0.123 [38]; μ is the shear modulus, obtained by mixing pure elements; ν = 0.24 is the Poisson ratio from the FeCrNi alloy at 293 K [39]; $b = \sqrt{2}/2\ a$ which is the Burgers vector from previous studies; a is the lattice constant of the FCC matrix [11]; $f_1(w_c)$ = 0.35; $f_2(w_c)$ = 5.70; c_n is the molar ratio of each element in the alloy; $\sigma_{\Delta V_n}$ is the standard deviation caused by local fluctuations, which can be ignored in the calculation; $\Delta \overline{V}_n$ is the average misfit volume; and $\Delta \overline{V}_n = V_n - \overline{V}$, $\overline{V} = \sum_n c_n V_n$. The atomic volumes ($V_n$) of Fe, Ni, Mn, Cr, and Al are 12.09, 10.94, 12.6, 12.27, and 14.3 $Å^3$, respectively [36].

Finally, the solid solution strengthening of the R1273 and R1473 alloys was calculated to be 92 MPa and 161 MPa, respectively. Combined with the grain boundary strengthening observed in the previous study, the calculated yield strengths at room temperature were 182 MPa and 253 MPa, which closely match the experimental values of 190 MPa and 255 MPa, respectively. Similarly, other temperature values were fitted. The constant term of the fitting function in Figure 8a–c represents the combined effect of various strengthening mechanisms, excluding solid solution strengthening. The fitting accuracy of the R1473 and A973 alloys is poorer, which may be attributed to the presence of a secondary phase.

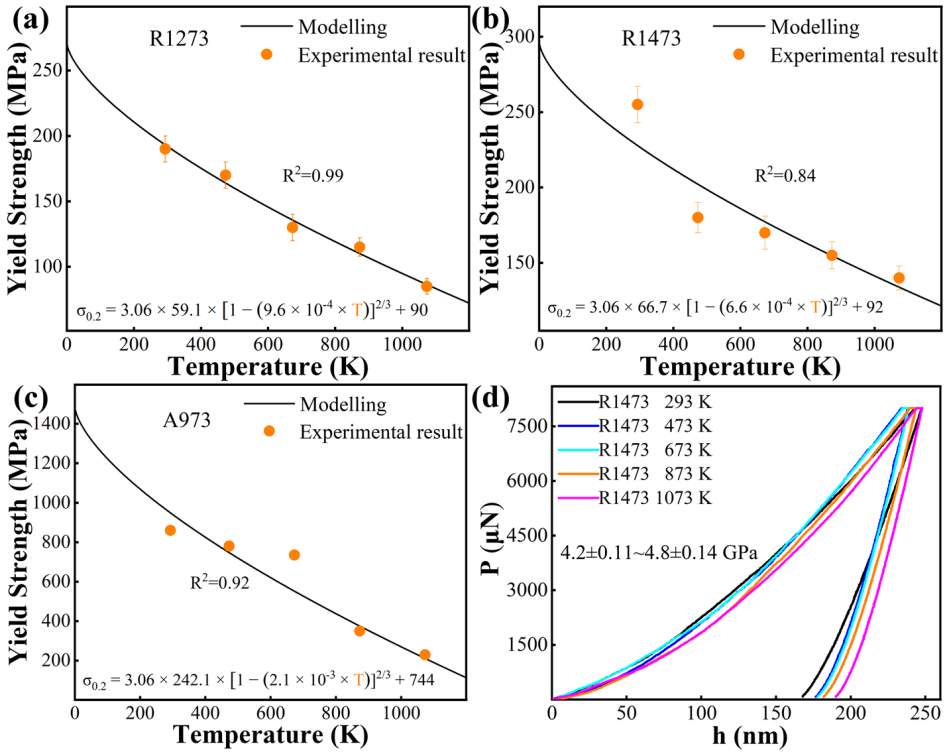

Figure 8. (**a**–**c**) Comparison of yield strength fitting results with experimental values for R1273, R1473, and A973 alloys at different temperatures; (**d**) the representative load–displacement (*P*-*h*) curves of the bulk NiAl-B2 phase in the R1473 alloy at various temperatures.

Another classical Zerilli–Armstrong (Z-A) model can also predict the yield strength of materials at different strain rates or temperatures [40]. It is a macroscopic predictive constitutive model based on physical principles. The expression is as follows:

$$\sigma_y = c_1 \varepsilon^{1/2} exp\left(-c_2 T + c_3 T ln\dot{\varepsilon}\right) + \sigma_G \quad (4)$$

where c_1, c_2, and c_3 are material parameters; ε is taken as 0.002; $\dot{\varepsilon}$ is 10^{-3} s^{-1}; T is the thermodynamic temperature; and σ_G is the adiabatic stress, which can be recognized as the grain boundary strengthening effect of the recrystallized alloy. Taking the R1273 alloy as an example, the material parameters in Equation (4) were fitted using the yield stresses at temperatures of 77, 473, 873, and 1073 K. The fitted values of c_1, c_2, and c_3 were 6610 MPa, 8.2×10^{-3} K^{-1}, and 7.38×10^{-4} K^{-1}, respectively. The coefficient of determination was 0.97 (R^2 = 0.97). The fitting equation predicted that the yield strength of the alloy at 293 K was 209 MPa and the yield strength of the alloy at 673 K was 127 MPa, which is in good agreement with the experimental values. The Z-A model also provides a good description of the yield strength of single-phase alloys as a function of temperature. The effect of second-phase particles at different temperatures remains unknown.

Both the strength of the precipitated phase and the phase interface introduce effects. It is impossible to quantitatively calculate the change in phase interface interaction force

with temperature. However, it is possible to test the microhardness of the heated bulk second phase in order to determine the effect of the precipitated phase. The representative load–displacement (*P-h*) curves of the bulk NiAl-B2 phase in the R1473 alloy at various temperatures are depicted in Figure 8. Nanoindentation results indicate the characteristics of the microstructure [16]. The hardness of the secondary phase decreases less as the temperature increases. Thus, the uncertain factors in the model arise from the two-phase interface. Chou et al. revealed that the strengthening effect of hetero-grain/precipitation engineering begins to decline after 673 K [20]. There is a sudden decrease in the interaction force between the second-phase particles and the matrix. This is consistent with the softening of the A973 alloy at 773 K. However, this section cannot be quantitatively analyzed at this time.

The contribution of the aluminum element to the matrix is mainly in solid solution strengthening. At the same time, the addition of the element Al improves the oxidation resistance and promotes type-B serration behavior, thereby improving the strain-hardening capability of the alloy. The high density of precipitates allows the alloy to maintain excellent mechanical properties at 673 K. Furthermore, the weakening of phase interface interactions should help to alleviate stress concentrations. The plasticity of A973 alloy has been slightly improved. Therefore, the A973 alloy is superior below 673 K.

5. Conclusions

In this study, the temperature sensitivity of different components and microstructures was analyzed by examining the high-temperature mechanical behavior of $Fe_{45}Mn_{15}Cr_{15}Ni_{25}$ and $Fe_{35}Mn_{15}Cr_{15}Ni_{25}Al_{10}$ high-entropy alloys. The properties were correlated with the results of the tensile test and fracture characteristics.

(1) The serration features, ranging from type-A, A + B, B, to C, are observed in the recrystallization alloy doped with Al between 473 K and 873 K. However, the $Fe_{45}Mn_{15}Cr_{15}Ni_{25}$ alloy only exhibits type-A serrations at 673 K. This suggests that the presence of Al intensifies solute–dislocation interactions and enhances the strain-hardening ability of the alloy. The appearance of type-B serrations delays the reduction in plasticity in the R1473 alloy.

(2) Intergranular fracture and oxidation can cause medium-temperature embrittlement of the recrystallized alloy at 873 K. This indicates that the hot working temperature of the studied alloy should be below 873 K.

(3) The aged $Fe_{35}Mn_{15}Cr_{15}Ni_{25}Al_{10}$ alloy maintains excellent mechanical properties at 673 K, with a yield strength of 735 MPa, ultimate tensile strength of 1030 MPa, and elongation of 11%. However, the force at the two-phase interface decreases, causing the softening temperature of the alloy to advance to 773 K. The high-temperature (>673 K) stability of high-strength alloys containing semi-coherent precipitated particles is unsatisfactory.

(4) The variation in yield strength with temperature can be described by the solid solution strengthening model proposed by Varvenne et al. The prediction accuracy of the single-phase alloy is higher than that of dual-phase alloys. The temperature sensitivity of grain boundary strengthening and precipitation strengthening is minimal, but the interface force is significantly affected by temperature. This method can be used to predict the mechanical properties of alloys at different temperatures and provide processing parameters.

Supplementary Materials: The following supporting information can be downloaded at: https://www.mdpi.com/article/10.3390/met13111885/s1, Table S1: Composition, experimental temperatures, and tensile properties of the reported alloys.

Author Contributions: Conceptualization, data curation, writing—original draft, D.L.; software, formal analysis, writ-ing—review and editing, X.J.; writing—review and editing, H.Y.; conceptualization, writing—review and editing, project administration, J.Q.; writing—review and editing, Y.Z. All authors have read and agreed to the published version of the manuscript.

Funding: This research was funded by the National Natural Science Foundation of China (no. 52271110 and no. 52301217), the Natural Science Foundation of Shanxi Province, China (no. 20210302124043 and no. 20210302124427) and the Key Research and Development Program of Shanxi Province (no. 202102050201008).

Data Availability Statement: The data that support the findings of this study are available from the corresponding author upon reasonable request.

Acknowledgments: The authors would like to acknowledge the support of the National Natural Science Foundation of China (no. 52271110), the Natural Science Foundation of Shanxi Province, China (no. 20210302124043 and no. 20210302124427) and the Key Research and Development Program of Shanxi Province (no. 202102050201008). Xi Jin would like to acknowledge the financial support of the National Natural Science Foundation of China (no. 52301217). Thanks to Wenjie Lin for his support in providing resources and curating data.

Conflicts of Interest: The authors declare no conflict of interest.

References

1. Cantor, B.; Chang, I.T.H.; Knight, P.; Vincent, A.J.B. Microstructural development in equiatomic multicomponent alloys. *Mater. Sci. Eng. A* **2004**, *375–377*, 213–218. [CrossRef]
2. Yeh, J.W.; Chen, S.K.; Lin, S.J.; Gan, J.Y.; Chin, T.S.; Shun, T.T.; Tsau, C.H.; Chang, S.Y. Nanostructured High-Entropy Alloys with Multiple Principal Elements: Novel Alloy Design Concepts and Outcomes. *Adv. Eng. Mater.* **2004**, *6*, 299–303. [CrossRef]
3. Li, Z.; Zhao, S.; Ritchie, R.O.; Meyers, M.A. Mechanical properties of high-entropy alloys with emphasis on face-centered cubic alloys. *Prog. Mater. Sci.* **2019**, *102*, 296–345. [CrossRef]
4. George, E.P.; Curtin, W.A.; Tasan, C.C. High entropy alloys: A focused review of mechanical properties and deformation mechanisms. *Acta Mater.* **2020**, *188*, 435–474. [CrossRef]
5. Gludovatz, B.; Hohenwarter, A.; Catoor, D.; Chang, E.H.; George, E.P.; Ritchie, R.O. A fracture-resistant high-entropy alloy for cryogenic applications. *Science* **2014**, *345*, 1153–1158. [CrossRef]
6. Sun, S.J.; Tian, Y.Z.; An, X.H.; Lin, H.R.; Wang, J.W.; Zhang, Z.F. Ultrahigh cryogenic strength and exceptional ductility in ultrafine-grained CoCrFeMnNi high-entropy alloy with fully recrystallized structure. *Mater. Today Nano* **2018**, *4*, 46–53. [CrossRef]
7. Han, Z.; Ren, W.; Yang, J.; Du, Y.; Wei, R.; Zhang, C.; Chen, Y.; Zhang, G. The deformation behavior and strain rate sensitivity of ultra-fine grained CoNiFeCrMn high-entropy alloys at temperatures ranging from 77 K to 573 K. *J. Alloys Compd.* **2019**, *791*, 962–970. [CrossRef]
8. Sun, J.; Zhao, W.; Yan, P.; Li, S.; Dai, Z.; Jiao, L.; Qiu, T.; Wang, X. High temperature tensile properties of as-cast and forged CrMnFeCoNi high entropy alloy. *Mater. Sci. Eng. A* **2022**, *850*, 143570. [CrossRef]
9. Zhang, P.; Wang, S.; Lin, Z.; Yue, X.; Gao, Y.; Zhang, S.; Yang, H. Investigation on the mechanism of micro-milling CoCrFeNiAlX high entropy alloys with end milling cutters. *Vacuum* **2023**, *211*, 111939. [CrossRef]
10. Lai, L.; Gan, M.; Wang, J.; Chen, L.; Liang, X.; Feng, J.; Chong, X. New class of high-entropy rare-earth niobates with high thermal expansion and oxygen insulation. *J. Am. Ceram. Soc.* **2023**, *106*, 4343–4357. [CrossRef]
11. Liu, D.; Hou, J.; Jin, X.; Wang, X.; Yang, H.; Qiao, J. The cobalt-free $Fe_{35}Mn_{15}Cr_{15}Ni_{25}Al_{10}$ high-entropy alloy with multiscale particles for excellent strength-ductility synergy. *Intermetallics* **2023**, *163*, 108064. [CrossRef]
12. Zhao, Y.L.; Yang, T.; Zhu, J.H.; Chen, D.; Yang, Y.; Hu, A.; Liu, C.T.; Kai, J.J. Development of high-strength Co-free high-entropy alloys hardened by nanosized precipitates. *Scr. Mater.* **2018**, *148*, 51–55. [CrossRef]
13. Stepanov, N.D.; Shaysultanov, D.G.; Chernichenko, R.S.; Tikhonovsky, M.A.; Zherebtsov, S.V. Effect of Al on structure and mechanical properties of Fe-Mn-Cr-Ni-Al non-equiatomic high entropy alloys with high Fe content. *J. Alloys Compd.* **2019**, *770*, 194–203. [CrossRef]
14. Li, J.; Gao, B.; Tang, S.; Liu, B.; Liu, Y.; Wang, Y.; Wang, J. High temperature deformation behavior of carbon-containing FeCoCrNiMn high entropy alloy. *J. Alloys Compd.* **2018**, *747*, 571–579. [CrossRef]
15. Niu, B.; Wang, Z.; Wang, Q.; Ge, S.; Dong, C.; Zhang, R.; Liu, H.; Liaw, P.K. Effect of Zr addition on the stability of precipitated Laves phase and mechanical properties of Fe–Cr–Al-based alloys at high temperatures. *Prog. Nat. Sci. Mater. Int.* **2022**, *32*, 114–127. [CrossRef]
16. Guo, Q.; Hou, H.; Pan, Y.; Pei, X.; Song, Z.; Liaw, P.K.; Zhao, Y. Hardening-softening of $Al_{0.3}$CoCrFeNi high-entropy alloy under nanoindentation. *Mater. Des.* **2023**, *231*, 112050. [CrossRef]
17. Wang, X.; Li, X.; Xie, H.; Fan, T.; Zhang, L.; Li, K.; Cao, Y.; Yang, X.; Liu, B.; Bai, P. Effects of Al and La elements on mechanical properties of $CoNiFe_{0.6}Cr_{0.6}$ high-entropy alloys: A first-principles study. *J. Mater. Res. Technol.* **2023**, *23*, 1130–1140. [CrossRef]
18. He, J.Y.; Liu, W.H.; Wang, H.; Wu, Y.; Liu, X.J.; Nieh, T.G.; Lu, Z.P. Effects of Al addition on structural evolution and tensile properties of the FeCoNiCrMn high-entropy alloy system. *Acta Mater.* **2014**, *62*, 105–113. [CrossRef]
19. Li, Y.; Zhou, J.; Liu, Y.; Lu, C.; Shi, L.; Zheng, W.; Jin, W.; Gao, Z.; Yang, J.; He, Y. Microstructural evolution and mechanical characterization for the $AlCoCrFeNi_{2.1}$ eutectic high-entropy alloy under different temperatures. *Fatigue Fract. Eng. Mater. Struct.* **2023**, *46*, 1881–1892. [CrossRef]

20. Chou, T.H.; Li, W.P.; Chang, H.W.; Cao, B.X.; Luan, J.H.; Huang, J.C.; Yang, T. Suppressing temperature-dependent embrittlement in high-strength medium-entropy alloy via hetero-grain/precipitation engineering. *Scr. Mater.* **2023**, *229*, 115377. [CrossRef]
21. Ait-Amokhtar, H.; Fressengeas, C. Crossover from continuous to discontinuous propagation in the Portevin–Le Chatelier effect. *Acta Mater.* **2010**, *58*, 1342–1349. [CrossRef]
22. Carroll, R.; Lee, C.; Tsai, C.-W.; Yeh, J.-W.; Antonaglia, J.; Brinkman, B.A.W.; LeBlanc, M.; Xie, X.; Chen, S.; Liaw, P.K.; et al. Experiments and Model for Serration Statistics in Low-Entropy, Medium-Entropy and High-Entropy Alloys. *Sci. Rep.* **2015**, *5*, 16997. [CrossRef] [PubMed]
23. Tirunilai, A.S.; Sas, J.; Weiss, K.-P.; Chen, H.; Szabó, D.V.; Schlabach, S.; Haas, S.; Geissler, D.; Freudenberger, J.; Heilmaier, M.; et al. Peculiarities of deformation of CoCrFeMnNi at cryogenic temperatures. *J. Mater. Res.* **2018**, *33*, 3287–3300. [CrossRef]
24. Tirunilai, A.S.; Weiss, K.-P.; Freudenberger, J.; Heilmaier, M.; Kauffmann, A. Revealing the Role of Cross Slip for Serrated Plastic Deformation in Concentrated Solid Solutions at Cryogenic Temperatures. *Metals* **2022**, *12*, 514. [CrossRef]
25. Jiang, W.; Yuan, S.; Cao, Y.; Zhang, Y.; Zhao, Y. Mechanical properties and deformation mechanisms of a $Ni_2Co_1Fe_1V_{0.5}Mo_{0.2}$ medium-entropy alloy at elevated temperatures. *Acta Mater.* **2021**, *213*, 116982. [CrossRef]
26. de Oliveira, M.; Couto, A.; Almeida, G.; Reis, D.; de Lima, N.; Baldan, R. Mechanical Behavior of Inconel 625 at Elevated Temperatures. *Metals* **2019**, *9*, 301. [CrossRef]
27. Licavoli, J.J.; Gao, M.C.; Sears, J.S.; Jablonski, P.D.; Hawk, J.A. Microstructure and Mechanical Behavior of High-Entropy Alloys. *J. Mater. Eng. Perform.* **2015**, *24*, 3685–3698. [CrossRef]
28. Roy, A.K.; Venkatesh, A.; Marthandam, V.; Ghosh, A. Tensile Deformation of a Nickel-base Alloy at Elevated Temperatures. *J. Mater. Eng. Perform.* **2008**, *17*, 607–611. [CrossRef]
29. Yang, T.; Tang, Z.; Xie, X.; Carroll, R.; Wang, G.; Wang, Y.; Dahmen, K.A.; Liaw, P.K.; Zhang, Y. Deformation mechanisms of $Al_{0.1}$CoCrFeNi at elevated temperatures. *Mater. Sci. Eng. A* **2017**, *684*, 552–558. [CrossRef]
30. Otto, F.; Dlouhý, A.; Somsen, C.; Bei, H.; Eggeler, G.; George, E.P. The influences of temperature and microstructure on the tensile properties of a CoCrFeMnNi high-entropy alloy. *Acta Mater.* **2013**, *61*, 5743–5755. [CrossRef]
31. Cao, B.X.; Wei, D.X.; Zhang, X.F.; Kong, H.J.; Zhao, Y.L.; Hou, J.X.; Luan, J.H.; Jiao, Z.B.; Liu, Y.; Yang, T.; et al. Intermediate temperature embrittlement in a precipitation-hardened high-entropy alloy: The role of heterogeneous strain distribution and environmentally assisted intergranular damage. *Mater. Today Phys.* **2022**, *24*, 100653. [CrossRef]
32. Gardner, L.; Insausti, A.; Ng, K.T.; Ashraf, M. Elevated temperature material properties of stainless steel alloys. *J. Constr. Steel Res.* **2010**, *66*, 634–647. [CrossRef]
33. Senkov, O.N.; Scott, J.M.; Senkova, S.V.; Meisenkothen, F.; Miracle, D.B.; Woodward, C.F. Microstructure and elevated temperature properties of a refractory TaNbHfZrTi alloy. *J. Mater. Sci.* **2012**, *47*, 4062–4074. [CrossRef]
34. Eleti, R.R.; Chokshi, A.H.; Shibata, A.; Tsuji, N. Unique high-temperature deformation dominated by grain boundary sliding in heterogeneous necklace structure formed by dynamic recrystallization in HfNbTaTiZr BCC refractory high entropy alloy. *Acta Mater.* **2020**, *183*, 64–77. [CrossRef]
35. Varvenne, C.; Luque, A.; Curtin, W.A. Theory of strengthening in fcc high entropy alloys. *Acta Mater.* **2016**, *118*, 164–176. [CrossRef]
36. Zhang, D.D.; Wang, H.; Zhang, J.Y.; Xue, H.; Liu, G.; Sun, J. Achieving excellent strength-ductility synergy in twinned NiCoCr medium-entropy alloy via Al/Ta co-doping. *J. Mater. Sci. Technol.* **2021**, *87*, 184–195. [CrossRef]
37. Leyson, G.P.; Curtin, W.A.; Hector, L.G., Jr.; Woodward, C.F. Quantitative prediction of solute strengthening in aluminium alloys. *Nat. Mater.* **2010**, *9*, 750–755. [CrossRef]
38. Szajewski, B.A.; Pavia, F.; Curtin, W.A. Robust atomistic calculation of dislocation line tension. *Model. Simul. Mater. Sci. Eng.* **2015**, *23*, 085008. [CrossRef]
39. Laplanche, G.; Gadaud, P.; Bärsch, C.; Demtröder, K.; Reinhart, C.; Schreuer, J.; George, E.P. Elastic moduli and thermal expansion coefficients of medium-entropy subsystems of the CrMnFeCoNi high-entropy alloy. *J. Alloys Compd.* **2018**, *746*, 244–255. [CrossRef]
40. Zerilli, F.J.; Armstrong, R.W. Dislocation-mechanics-based constitutive relations for material dynamics calculations. *J. Appl. Phys.* **1987**, *61*, 1816–1825. [CrossRef]